Materials and Design 91 (2016) 278–285

Contents lists available at ScienceDirect

Materials and Design

journal homepage: www.elsevier.com/locate/matdes

Effect of composition on tensile properties and fracture toughness of Al–Zn–Mg alloy (A7N01S-T5) used in high speed trains

C. Qin [a], G.Q. Gou [a,*], X.L. Che [a], H. Chen [a], J. Chen [a,b], P. Li [c], W. Gao [d]

[a] School of Materials Science and Engineering, Southwest Jiaotong University, Chengdu 610031, China
[b] Chengdu Industry and Trade College, Chengdu 611731, China
[c] CSR Qingdao Sifang Co. Ltd., Qingdao 266000, China
[d] Department of Chemical & Materials Engineering, The University of Auckland, Auckland 1142, New Zealand

ARTICLE INFO

Article history:
Received 11 October 2015
Received in revised form 18 November 2015
Accepted 27 November 2015
Available online 02 December 2015

Keywords:
A7N01S-T5 aluminum alloy
Alloy composition
Microstructure
Tensile properties
Fracture toughness
High speed train

ABSTRACT

The Al–Zn–Mg aluminum alloy A7N01S-T5 used in high speed trains was designed by orthogonal method. The effect of elemental composition on the tensile properties and fracture toughness has been investigated. The alloys with different compositions were tested by tensile and three point bending tests: the range analysis results showed that the compositions of Zn and Mg were the main factors that affect the strength and plasticity of the alloys. The tensile testing results showed that the #1 alloy Al-4.34Zn-1.43 Mg-0.27Mn-0.13Cr-0.12Zr-0.07Ti had the best combination of tensile strength, yield strength and elongation, which were 415 MPa, 378 MPa and 13.5%, respectively. Furthermore, this alloy showed the excellent ability to hinder the crack propagation with a value of $J_{0.2BL(12)} = 23.37\ kJ \cdot m^{-2}$. The microstructure, grain size, compositions and fracture characteristics of the alloy were investigated by optical microscopy (OM), scanning electron microscopy (SEM), energy dispersive spectrometer (EDS), backscattered electron diffraction (EBSD) and transmission electron microscopy (TEM). The results indicated that the strength is mainly determined by the volume fraction, size and distribution of precipitated $\eta'(MgZn_2)$ phase. The discontinuous distribution of $\eta(MgZn_2)$ phase, narrow precipitated-free zones (PFZs) and fine grain size played important roles to obtain high fracture toughness.

1. Introduction

A7N01S-T5 aluminum alloy belongs to the Al–Zn–Mg alloy series. It has been widely used in high-speed train bodies and welding structures, such as corbels, beams and underframes due to its high strength, low density and good welding properties [1,2]. In addition to Al and the main alloying elements for Zn and Mg, A7N01S-T5 alloy contains minority elements and impurity elements, such as Mn, Cr, Zr, Ti, Fe and Si. It has generally been recognized that alloying composition and treatment determine the grain type, grain size, and distribution of precipitated phase, which affect the strength and fracture toughness of the alloy [3,4].

As Zn and Mg are the main alloying elements of 7xxx series alloys, much effort has been made to investigate the fine-scale precipitation of metastable Zn- and Mg-rich $\eta'(MgZn_2)$ phase and its precursors in 7xxx series alloys [5,6]. It has been reported that an increase of Zn and Mg contents results in increasing volume fraction of metastable precipitates and improvement of alloy strength [7,8].

Studies also revealed that minority elements such as Ti, Zr, Cr, and Mn can form different dispersoids and microstructures which affect the mechanical properties of Al–Zn–Mg alloys. A study on optimized Ti and Zr content in high strength 7xxx alloys has been reported and the research revealed that the Ti-refined alloys possess higher tensile strength and elongation [9]. Minor Zr additives help in precipitating primary Al_3Zr particles from the molten pool during solidification, and the particles promote α-Al nucleation [10–13]. This mechanism can improve the alloy strength, decrease the susceptibility of stress corrosion cracking and restrict the nucleation of recrystallization [14–16]. Studies also showed that adding Cr can inhibit the recrystallization of Al–Zn–Mg–Cu–Zr alloys, greatly enhancing mechanical properties and fracture toughness as well as the resistance for stress corrosion cracking [17–19]. Adding Mn can form Al_6Mn in Al–Zn–Mg matrix which can increase the strength without scarifying plasticity due to the dispersion hardening effects [20–22]. Moreover, Cr and Mn decrease the surface tension between liquid Al and solid Al_3Ti, Al_3Zr and $Al_3(Ti_x,Zr_{1-x})$ particles, therefore impeding the nucleation and growth of particles [23].

Although extensive studies on one or two elements have been made to affect various mechanical properties and microstructural changes in Al–Zn–Mg alloys, published work on multiple elements of the same is rather limited. In this paper, the elements which have a similar effect on the properties would be taken into consideration as the same one factor. Then three combinations of alloying elements, Zn and Mg, Mn and Cr, and Zr and Ti, were used to design alloys by the orthogonal array $L_4(2^3)$. We report our investigation on the effect of composition

* Corresponding author.
E-mail address: gouguoqing@swjtu.cn (G.Q. Gou).

http://dx.doi.org/10.1016/j.matdes.2015.11.107
0264-1275/

on tensile properties and fracture toughness of Al–Zn–Mg alloy A7N01S-T5.

2. Materials and experimental work

2.1. Materials

The orthogonal designing level for elemental composition is presented in Table 1, and it was designed that the real composition must meet with the compositions in the bracket. Four types of 12 mm thick aged Al–Zn–Mg alloys (A7N01) with T5 aging were provided by Longkou Conglin Aluminum Co., LTD. Four types of alloys were named as #1, #2, #3 and #4. The chemical composition of the alloys, analyzed by arc-spark direct reading spectrometer, is given in Table 2.

The alloys were melted in an electrical-resistance furnace and casted into an iron mold with internal dimensions of 480 mm. The as-cast ingots were homogenized at 455 ± 5 °C for 16 h, followed by air cooling in room temperature. Then the ingots were converted into aluminum alloy sections by hot extrusion at 520 ± 10 °C, with an extrusion ratio of 19.4:1. After extrusion, the materials without solution treatment were cooled in air. The sections were aged at 105 °C and 150 °C separately for 10 h for T5-tempered according to ISO 2107:2007.

2.2. Mechanical properties tests and microstructural characterization

Samples that were used for tensile test were prepared after 12 month natural aging. The longitudinal direction of tensile samples was perpendicular to the rolling direction X. The tensile tests were conducted at the loading speed of 2 mm/min on a WDW-3100 electronic universal testing machine according to ISO 6892-1:2009.

Fracture toughness tests were carried out according to CMT-4304 by three point bending method on the fatigue pre-cracked samples of Y–X orientations, under a constant displacement velocity of 0.5 mm/min and span of 96 mm. Fig. 1 showed the shape and sizes of the samples which follow ISO 12135:2002. The J-Δa resistance curves were drawn after tests. Representative fracture surface microstructures of the bending samples were examined by SEM (JSM-6490LV).

The samples that were used for optical microscopy observations were prepared by Keller reagent (1% HF + 1.5% HCl + 2.5% HNO_3 + 95% H_2O). The grain morphology and size of samples were also observed by using electron back scattered diffraction on FEM-6500. The precipitations were investigated by TEM (JEM-2010). Thin foils for TEM analysis were prepared by twin-jet polishing with an electrolyte solution consisting of 25 vol.% HNO_3 and 75 vol.% methanol.

3. Results

3.1. Tensile properties and fracture toughness

The tensile properties of 4 alloys are shown in Fig. 2. The #3 alloy had the highest strength with 436 MPa of tensile strength and 405 MPa of yield strength. The #2 alloy had the highest elongation rate of 14.98%. #1 and #4 alloys were close in tensile strength and yield strength, but #1 alloy exhibited higher elongation than #4 alloy.

Fig. 3 shows the J-Δa resistance curves of 4 alloys. To make the 0.2 mm offset line intersecting with the J-Δa resistance curves, the

Table 2
Elemental composition of test A7N01S-T5 alloys (wt.%).

Sample No.	Si	Fe	Cu	Factor A		Factor B		Factor C		Al
				Zn	Mg	Mn	Cr	Zr	Ti	
#1	0.11	0.15	0.08	4.34	1.43	0.27	0.13	0.12	0.07	Bal.
#2	0.09	0.15	0.08	4.33	1.47	0.36	0.24	0.16	0.03	Bal.
#3	0.08	0.16	0.08	4.69	1.63	0.22	0.14	0.17	0.03	Bal.
#4	0.09	0.16	0.07	4.54	1.59	0.34	0.24	0.13	0.09	Bal.

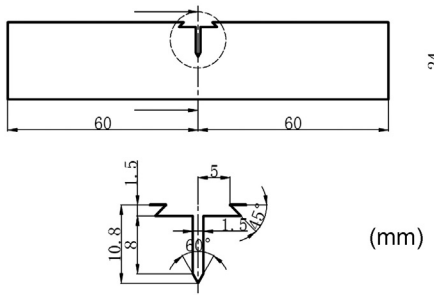

Fig. 1. Schematic diagram of samples size for fracture toughness test.

$J_{0.2BL(12)}$ was 23.37 kJ·m^{-2} for #1 alloy, 34.18 kJ·m^{-2} for #2 alloy, 14.24 kJ·m^{-2} for #3 alloy and 23.19 kJ·m^{-2} for #4 alloy. It can be concluded that #2 alloy has the best fracture toughness and #3 alloy has the worst value.

3.2. Orthogonal experiment results

The orthogonal experiment results with three factors and two levels were analyzed by range analysis method, and the results are presented in Table 3.

The results in Table 3 show that the change of R_m was in accordance with $R_{0.2}$. The strength increased with increasing Zn and Mg contents, decreasing Mn and Cr contents, and increasing Zr and Ti contents. In addition, the change of A was in accordance with $J_{0.2BL(12)}$. The plasticity increased with decreasing Zn and Mg contents, increasing Mn and Cr contents, and increasing Zr and Ti contents. Besides, the compositions of Zn and Mg were the main factors that affect the strength and plasticity of the alloys.

3.3. Fracture microstructure

The surface microstructures of the fracture samples are shown in Fig. 4. It can be seen that the failure mechanism of #1 alloy was mainly the transgranular fracture. There were some Fe-rich phase particles (Fig. 4a) in the center of the dimples and some of them were broken. The failure mechanism of #2 alloy was also the transgranular fracture but more and larger dimples distributed deeper in the fracture surface than those in #1 alloy. The failure mechanisms of #3 and #4 alloys were the intergranular and transgranular fracture. While the intergranular fracture was dominant in #3 alloy, and transgranular fracture was dominant in #4 alloy. Some secondary

Table 1
The orthogonal designing level for elemental composition of A7N01S-T5 alloys (wt.%).

Level	Factor A		Factor B		Factor C	
	Zn	Mg	Mn	Cr	Zr	Ti
1	4.35 (4.20–4.50)	1.50 (1.40–1.60)	0.25 (0.20–0.35)	0.15 (0.10–0.20)	0.12 (0.10–0.15)	0.08 (0.05–0.10)
2	4.65 (4.50–4.80)	1.70 (1.60–1.80)	0.40 (0.35–0.50)	0.25 (0.20–0.30)	0.18 (0.15–0.20)	0.03 (0–0.05)

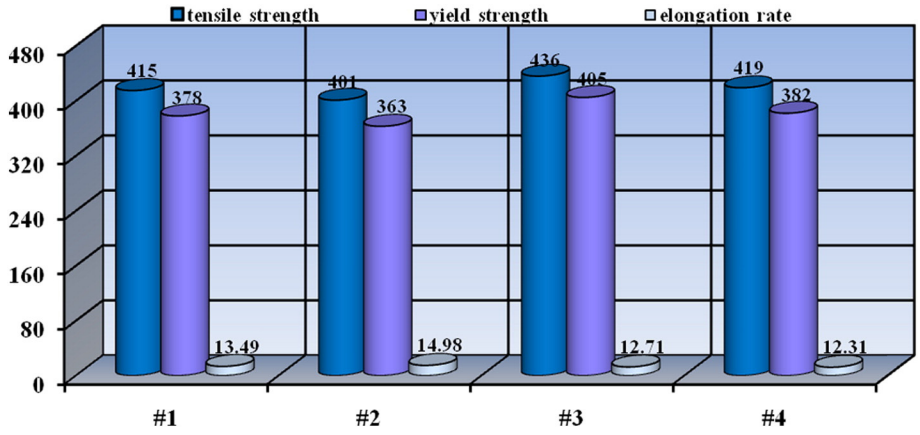

Fig. 2. Tensile properties of A7N01S-T5 alloys of different compositions.

cracks and subspheroidal second-phase particles were seen on the surface of #3 alloy (Fig. 4c).

3.4. Microstructure

Three directions of optical micrographs of A7N01S-T5 alloys with different compositions are presented in Fig. 5. There were many coarse recrystallized grains distributed in the microstructure of #1 alloy (Fig. 5a). Much more tiny grains and fiber-like un-recrystallized microstructures distributed along the rolling direction X in #2 alloy (Fig. 5b). The microstructures of #3 and #4 alloys were similar to #1, but some grains had a larger size. There were also distributed fiber-like unrecrystallized microstructures with fine sub-grains in #4 alloy (Fig. 5d).

The microstructures of SEM observations for the #2 alloy are shown in Fig. 5(e). It can be seen that a large amount of impurity-phase particles distributed inside the grains or on the grains boundaries. Besides, the impurity-phase particles with the size of 3–15 μm were mostly distributed at grain boundary areas, with the shape of short rod or irregular geometry. Coarse impurity-phases are generally detrimental to the toughness [5]. The other alloys had the same structure. It can be concluded that the Al, Zn, Mg, Fe, Mn and Cr were the main elements of impurity-phase particles from Fig. 5(f). So the impurity-phase particles may be (FeMn)Al_6, Al(FeMnCr), etc. More accurate compositions will need further analysis. For other particles the EDS analysis results were detected on a similar level.

The grain size distributions along X directions (Fig.5) are shown in Fig. 6 (different colors represent different grain sizes). The majority grains of #1 alloy were smaller than 90 μm with ~10% of grains in the range of 90–120 μm and ~46% grains in the range of 0–30 μm (Fig. 6a). Alloy #2 had a much smaller grain size than #1 with ~56% grains smaller than 30 μm (Fig. 6b). In alloy #3, 40% grains were greater than 90 μm, with ~19% grains in the range of 120–150 μm (Fig. 6c). The grain size of alloy #4 was similar to #3 alloy.

Typical TEM microstructures and select area electron diffraction (SAED) patterns of the grains and grain boundaries in the A7N01S-T5 alloys are shown in Fig. 7. Fig. 7a–d exhibits the small precipitates dispersed in the α-Al matrix, but the volume fraction, size and distribution pattern of precipitates were different. As shown in Fig. 4b, the corresponding electron diffraction of η′($MgZn_2$) precipitates could be identified at the positions of 1/3[422] and 2/3[422] in SAED of <111> direction of the Al alloy [24]. η′ phase is a metastable hexagonal phase, semi-coherent with the aluminum matrix, and is the main hardening precipitate in Al–Zn–Mg alloy [8]. Besides, secondary coherent Al_3Zr particles had a similar lattice parameter to α-Al matrix and appeared 1/2[220] of Fig. 4(b) and (d) with an ordered $L1_2$ cubic crystal structure [25]. The η′ phases are functionally important as well as

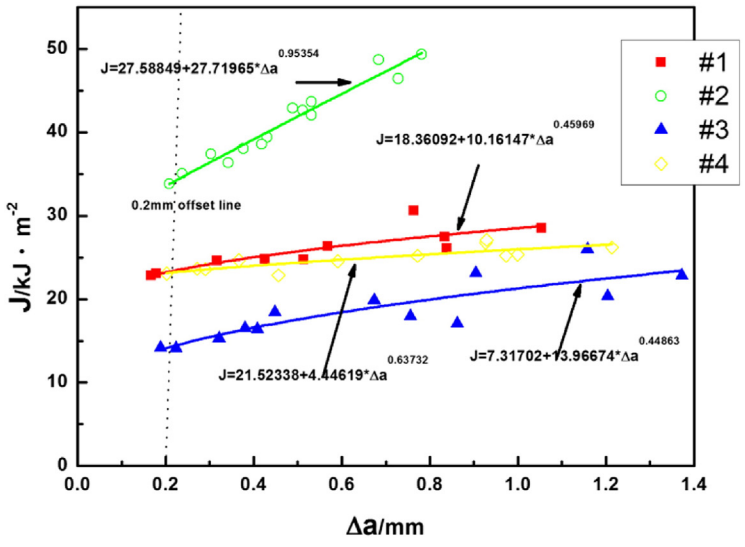

Sample No.	$J_{0.2BL(12)}$ /kJ·m^{-2}
#1	23.37
#2	34.18
#3	14.24
#4	23.19

Fig. 3. J-Δa resistance curves of four A7N01S-T5 alloys.

Table 3
Range analysis results.

Factor	Level	R_m /MPa	$R_{0.2}$ /MPa	A /%	$J_{0.2BL(12)}$ /kJ·m^{-2}
A	1	408	371	14.24	28.78
	2	428	394	12.51	18.71
B	1	426	392	13.10	18.80
	2	410	373	13.65	28.69
C	1	417	380	12.90	23.28
	2	419	384	13.85	24.21
Target component		A2B1C2 (#3)	A2B1C2 (#3)	A1B2C2 (#2)	A1B2C2 (#2)
Influence degree		A > B > C	A > B > C	A > C > B	A > B > C

secondary Al_3Zr particles in pinning up the dislocation and preventing the grain boundary migration under tensile condition, i.e. dislocation movement would consume more energy when crossing the second phases [3,14]. Moreover, other alloys had the same electron diffraction image. Figs. 7e–h shows that the short rods or disk-like equilibrium $\eta(MgZn_2)$ precipitates with the size of 15–50 nm were distributed at the grain boundary areas. Equilibrium η precipitates in #1 alloy discontinuously, and the precipitate free zones (PFZs) with the width of 80 ± 15 nm were observed. For #2 alloy, η precipitates with narrowing PFZs were small and the shape was close to spherical. For #3 alloy, equilibrium η precipitates distributed continuously, and PFZs were not clearly seen in the grains. For #4 alloy, the grain boundary precipitate was continuous in one section but the others were discontinuous. The PFZs of the former were not clear and those of the latter were distinct with the width of 70 ± 5 nm.

4. Discussion

4.1. Effect of microstructure on the strength

The precipitation sequence of the second phases in Al–Zn–Mg alloy can be given as follows: supersaturated solid solution (SSSa) → GP zones → metastable η′(MgZn2) → stable η(MgZn2) [26,27]. What is more, the GP zones and η′ phase precipitates are the strengthening phases. If the precipitates transformed gradually from the metastable η′ phase to the stable η phase, the strength will reduce in general [7].

Although the grain size of the alloys is a factor in the strength, the difference in strength of Al–Zn–Mg alloy A7N01S-T5 is mainly associated with the size, distribution and volume fraction of the η′ phase [5,12,19]. The η′ phases distributed dispersion with a larger amount and smaller size. The more significant the precipitation strength effect is, the higher the strength of the alloy is. Fig. 7(c) shows that the η′ phase distributed uniformly in the #3 alloy grains was in a large quantity with small size. It can be concluded that the #3 alloy had the highest strength. The quantity of η′ phase in #4 alloy was similar with that of #3 alloy, but they distributed unevenly, so the strength of #4 alloy was relatively low. The quantity of η′ phase in #1 alloy (Fig. 7a) was less than that of #4 alloy and the size was larger, but the dispersion degree was higher, so the strength had no obvious change. The quantity of η′ phase in #2 alloy (Fig. 7b) was small and the size was the largest, resulting in the lowest strength.

4.2. Effect of microstructure on the fracture toughness

The η′ precipitates along grain boundaries grow, aggregate, coarsen and accelerate the grain boundary precipitation during the aging process. Finally, distinctly coarse and discrete grain boundary precipitates η are formed [12]. The fracture toughness of the alloys has a close relationship with the grain boundary precipitates [28].

There were two types of precipitates: one exists in the grain boundary (continuous or rather discontinuous in this case) and the second mesh distribution close to grain boundary, which are presented in Fig. 7e–h. The η precipitate with the continuous mesh distribution is the most unfavorable factor for fracture toughness of the alloys and η precipitate with fine size and discontinuous distribution is beneficial to the fracture toughness of the alloys [7,26]. The finer the precipitated phase is and the greater the spacing is, the higher the fracture toughness of the alloy is. One of the reasons of the #3 and #4 alloys showing brittle fracture mechanism is that the η phase had continuous

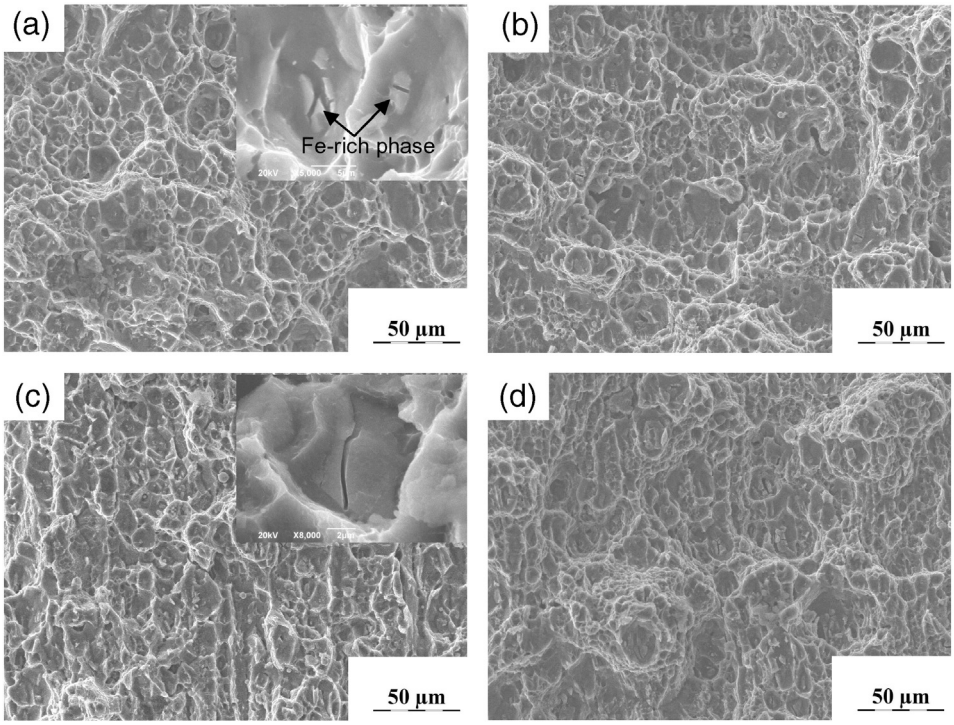

Fig. 4. Microstructure of fracture surface of different samples: (a) #1 (b) #2 (c) #3 (d) #4.

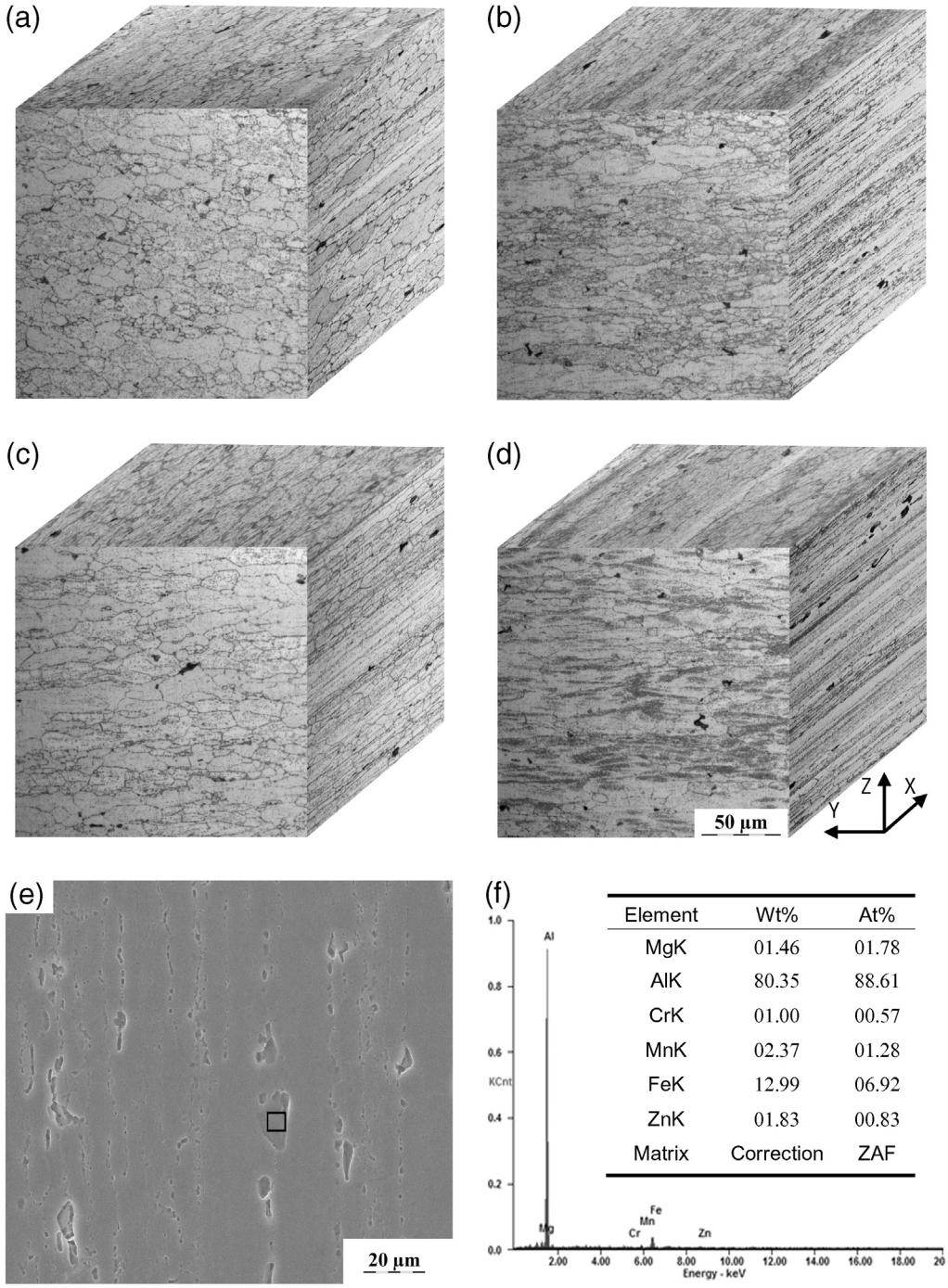

Fig. 5. Microstructures of A7N01S-T5 alloys at different compositions: (a) #1, (b) #2, (c) #3, (d) #4, SEM images (e) of #2 alloy and EDX results (f) of constituent particles.

mesh distribution (Fig. 7g and h). The PFZs are formed when the precipitation phases precipitate out in the grain boundary areas. This is the reason that the solute atoms distribute around the grain boundaries and the oversaturated vacancies diffuse to the grain boundary areas. When the thick precipitated phases formed in the grain boundary areas, the precipitation phases will not deposit out in both sides of the boundaries due to the dilution of solute atoms and vacancies [12]. The precipitated phase in the grain boundary is thicker and the PFZs are wider. Hence, the width of PFZs had a certain effect on the fracture toughness of materials: the wider the PFZs are, the poorer the fracture toughness of materials is.

Fig. 6 shows the different grain sizes of 4 alloys. We can see much tiny grains distributed along the rolling direction X and fiber-like un-recrystallized microstructure in #2 alloy (Fig. 5b). There is also a distributed fiber-like un-recrystallized microstructure with fine sub-grains in #4 alloy (Fig. 5d). The #2 and #4 alloys had higher content Mn and Cr elements, and the #2 alloy had higher Zr and Ti contents. Zr and Cr can restrict the nucleation of recrystallization. X.M. Li's work [19] evidenced that the recrystallized area fraction of Zr-containing alloys is less than that of Cr-containing alloys, being attributable to Zr reducing recrystallization more effectively than Cr. So the #2 alloys and the #4 alloys had fiber-like un-recrystallized

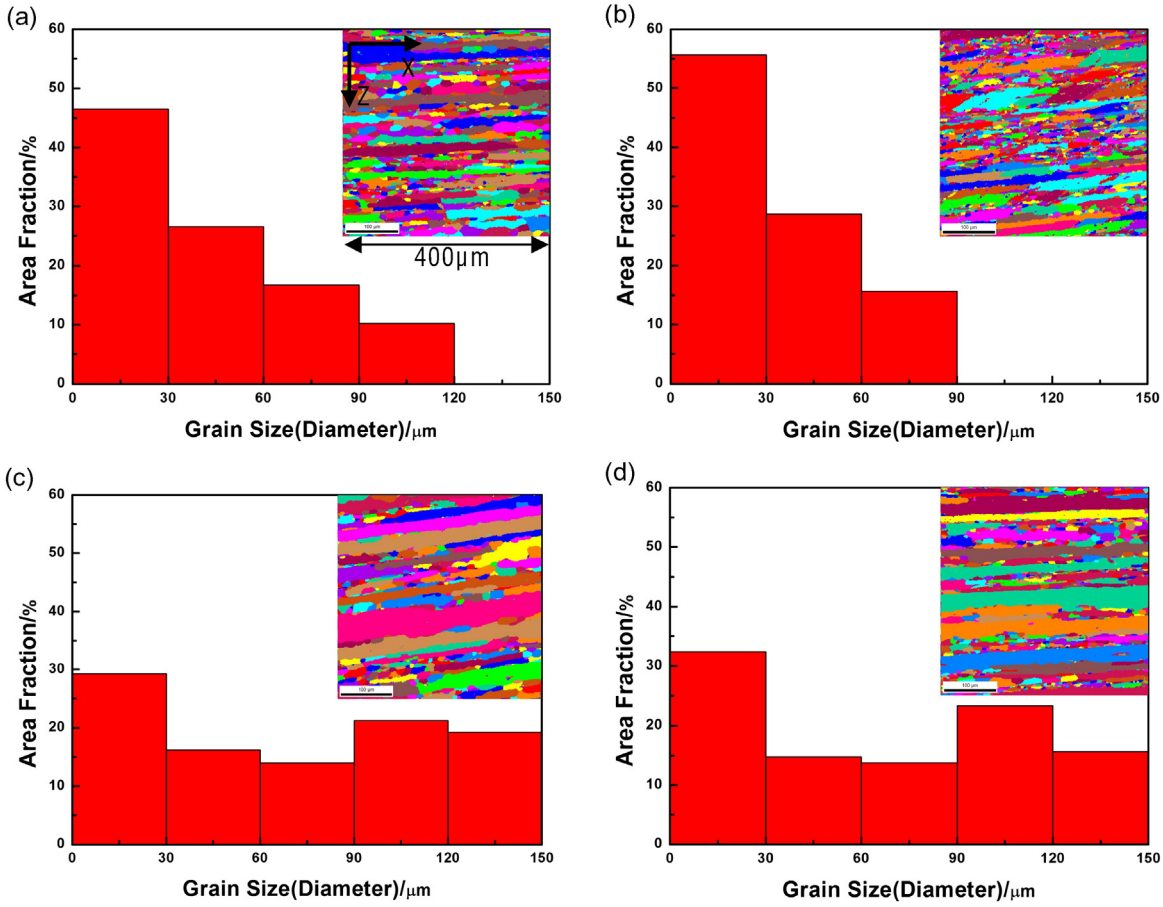

Fig. 6. Grain size distributions of A7N01S-T5 alloys at different compositions: (a) #1, (b) #2, (c) #3, (d) #4. (For interpretation of the references to color in this figure, the reader is referred to the web version of this article.)

microstructure, and the fiber-like un-recrystallized microstructure in #2 alloys distributed more than #4 alloy. The grain size is one of the causes that affect the fracture toughness of materials. In the process of crack propagation, the energy of plastic deformation is the key factor. Smaller grain size results in larger grain boundary areas (Fig. 8), therefore a higher fracture toughness.

The fracture toughness of 4 alloys was determined by both grain boundary of η precipitates and the grain size. The #3 alloy had the coarse and abnormally grown grains with continuous mesh distribution of η phase, so the fracture toughness was the lowest. The #4 alloy had the coarse grains, but η phase presented as the continuous and discontinuous precipitations, resulting in improved fracture toughness. Thus, the effect of grain boundary precipitation on the fracture toughness is dominant. The #1 alloy only had a small number of coarse grains; η phase presented discontinuous distribution, therefore possesses improved fracture toughness. The #2 alloy had fine grains and fine precipitation phase with higher spheroidization degree of η phase. This type of microstructure can reduce the stress concentration at the tip of the precipitated phase, resulting in intergranular fracture, therefore avoiding the premature crack nucleation in grain boundary areas with improved fracture toughness.

From the above analysis, we can see that the η phase distributed in the grain boundary areas played an important role on the fracture toughness of materials, especially when they form a continuous mesh-like structure. There may be two methods to control the formation and distribution of these precipitated phases. The first one is reducing the contents of Zn and Mg to as much as the required strength can be met, which can reduce the volume fraction of precipitates η in the grain boundary areas. The second is to optimize the aging process with lower temperature. The formation of a small amount of spherical precipitates in the grain boundary areas is beneficial to the fracture toughness of materials. This is because the intracrystalline atomic diffusion velocity is low at a low aging temperature, resulting in less precipitated phase formed in grain boundary areas. If we take the two methods, the alloy may obtain enough strength and fracture toughness [3,6,27].

4.3. The optimal level of composition

According to the results obtained from the orthogonal design method in Table 3, the effect of different factors on the mechanical properties and fracture toughness of alloy was complex. For the targeted parameters R_m and $R_{0.2}$, the composition which could obtain the maximum ratio was the #3 alloy, but its plasticity was relatively low, especially when it showed a brittle fracture failure. Although #2 alloy had the maximum A and $J_{0.2BL(12)}$, its strength was relatively low. Therefore the overall performance of #1 alloy is the best among the tested four alloys, although its composition may not reach the optimal level yet. More work on the composition optimization is in progress.

5. Conclusion

The Al–Zn–Mg alloy (A7N01S-T5) has been designed by using orthogonal method targeted for high speed train applications. The effects of compositions on the tensile strength and fracture

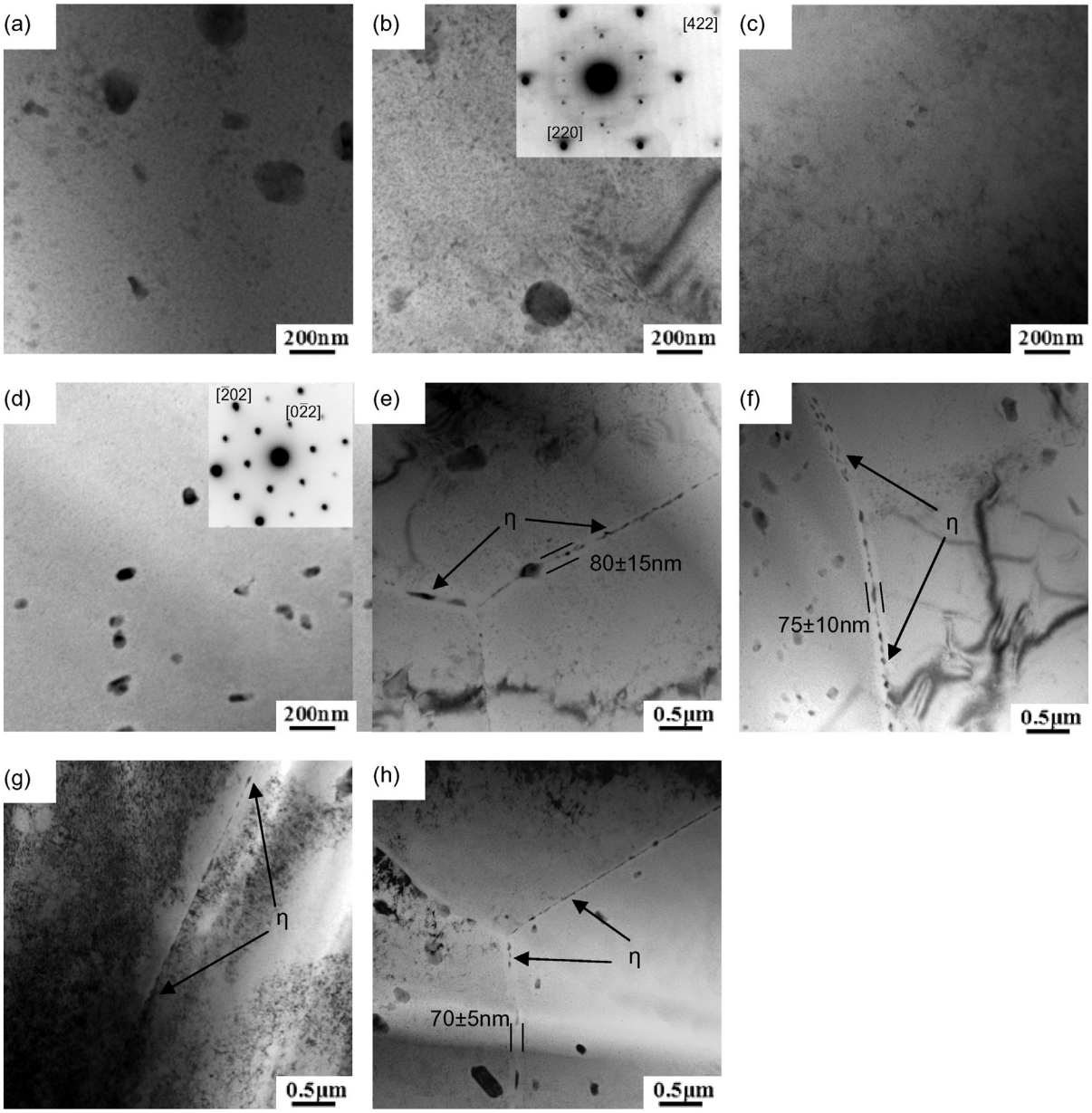

Fig. 7. TEM microstructures of A7N01S-T5 alloys at different compositions: and (e) #1, (b) and (f) #2, (c) and (g) #3, (d) and (h) #4.

toughness were investigated. The microstructure and fracture surface morphology were examined by various techniques. The following conclusions can be drawn out:

(1) The Al-4.34Zn-1.43 Mg-0.27Mn-0.13Cr-0.12Zr-0.07Ti (#1 alloy) had the best combination of mechanical properties. The tensile strength, yield strength and elongation rate of the alloy were 415 MPa, 378 MPa and 13.49%, respectively. Furthermore, this alloy showed the excellent ability to hinder the propagation of cracks with a value of $J_{0.2BL(12)} = 23.37\ kJ \cdot m^{-2}$.
(2) The change of R_m was in accordance with $R_{0.2}$ and the change of A was in accordance with $J_{0.2BL(12)}$. The contents of Zn and Mg were the main factors that affect the strength and plasticity of the alloys.
(3) The fracture toughness of four alloys was determined by both the grain size and η phase precipitation in the grain boundaries. The grain boundary precipitation showed a dominant effect on the fracture toughness of the alloys.

Acknowledgments

This work has been supported by the projects “Effect of residual stress on the corrosion behavior in weld joints and development of control technology for car bodies in aluminum-alloy trains”, “Research of the key technologies and equipment for next-generation railway transportation in cities” and “Basic research of the design and advanced welding technology for high speed trains in diverse environment”. The authors would like to acknowledge the financial support from the scientific and technological innovation projects, Chinese Central Universities (No. 2682014CX003), the National Science & Technology Pillar Program (No. 2015BAG12B01), and the preliminary research project of the National Key Basic Research and Development plan (No. 2014CB660807).

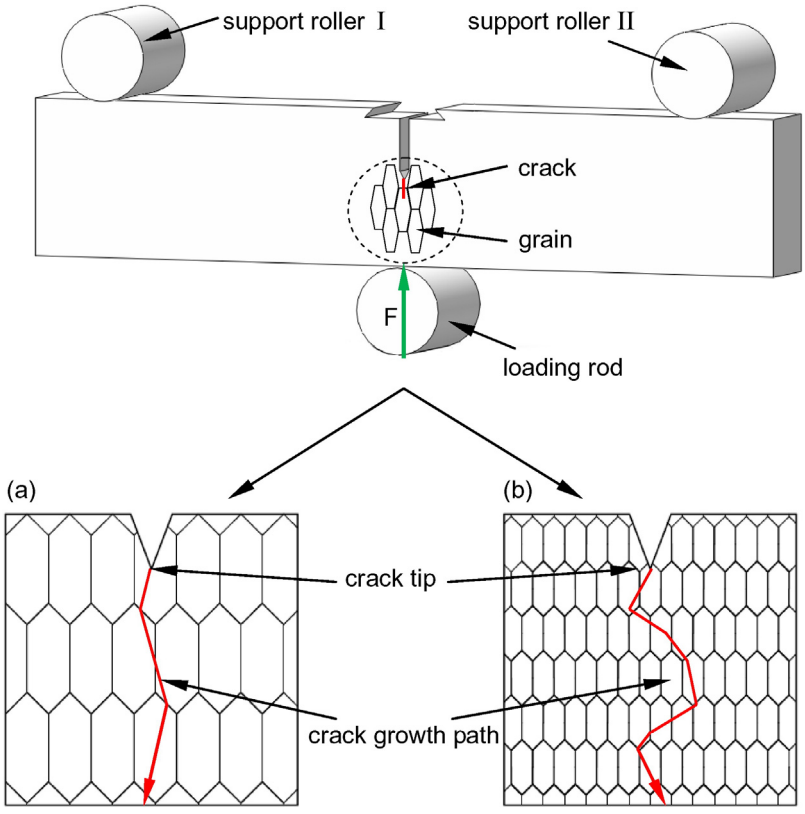

Fig. 8. The crack growth model of effect of grain size on fracture toughness: (a) big grain, (b) small grain.

References

[1] G. Gou, M. Zhang, H. Chen, J. Chen, P. Li, Y.P. Yang, Effect of humidity on porosity, microstructure, and fatigue strength of A7N01S-T5 aluminum alloy welded joints in high-speed trains, Mater. Design 85 (2015) 309–317.

[2] G.Q. Gou, N. Huang, H. Chen, H.M. Liu, A.Q. Tian, Z.C. Guo, Research on corrosion behavior of A6N01S-T5 aluminum alloy welded joint for high-speed trains, J. Mech. Sci. Technol. 26 (2012) 1471–1476.

[3] F. Wang, B.Q. Xiong, Y.Q. Zhang, B.H. Zhu, H.W. Liu, Z.X. Wang, et al., Microstructure and mechanical properties of spray-deposited Al-10.8Zn-2.8Mg-1.9Cu alloy after two-step aging treatment at 110 and 150 degrees C, Mater. Charact. 58 (2007) 82–86.

[4] C. Mondal, A.K. Mukhopadhyay, On the nature of T(Al2Mg3Zn3) and S(Al2CuMg) phases present in as-cast and annealed 7055 aluminum alloy, Mater. Sci. Eng. A-Struct. 391 (2005) 367–376.

[5] R. Ferragut, A. Somoza, A. Tolley, I. Torriani, Precipitation kinetics in Al–Zn–Mg commercial alloys, J. Mater. Process Technol. 141 (2003) 35–40.

[6] T. Engdahl, V. Hansen, P.J. Warren, K. Stiller, Investigation of fine scale precipitates in Al–Zn–Mg alloys after various heat treatments, Mater. Sci. Eng. A-Struct. 327 (2002) 59–64.

[7] X.Y. Sun, B. Zhang, H.Q. Lin, Y. Zhou, L. Sun, J.Q. Wang, et al., Correlations between stress corrosion cracking susceptibility and grain boundary microstructures for an Al–Zn–Mg alloy, Corros. Sci. 77 (2013) 103–112.

[8] Y.D. Jia, F.Y. Cao, Z.L. Ning, S. Guo, P. Ma, J.F. Sun, Influence of second phases on mechanical properties of spray-deposited Al–Zn–Mg–Cu alloy, Mater. Design 40 (2012) 536–540.

[9] N. Pourkia, M. Emamy, H. Farhangi, S.H.S. Ebrahimi, The effect of Ti and Zr elements and cooling rate on the microstructure and tensile properties of a new developed super high-strength aluminum alloy, Mater. Sci. Eng. A-Struct. 527 (2010) 5318–5325.

[10] X. Huang, Q.L. Pan, B. Li, Z.M. Liu, Z.Q. Huang, Z.M. Yin, Microstructure, mechanical properties and stress corrosion cracking of Al–Zn–Mg–Zr alloy sheet with trace amount of Sc, J. Alloys Compd. 650 (2015) 805–820.

[11] J.H. Li, M. Wiessner, M. Albu, S. Wurster, B. Sartory, F. Hofer, et al., Correlative characterization of primary Al-3(Sc,Zr) phase in an Al–Zn–Mg based alloy, Mater. Charact. 102 (2015) 62–70.

[12] C. Li, Q.L. Pan, Y.J. Shi, Y. Wang, B. Li, Influence of aging temperature on corrosion behavior of Al–Zn–Mg–Sc–Zr alloy, Mater. Design 55 (2014) 551–559.

[13] Y.J. Shi, Q.L. Pan, M.J. Li, X. Huang, B. Li, Effect of Sc and Zr additions on corrosion behaviour of Al–Zn–Mg–Cu alloys, J. Alloys Compd. 612 (2014) 42–50.

[14] Y. Deng, G.F. Xu, Z.M. Yin, X.F. Lei, J.W. Huang, Effects of Sc and Zr microalloying additions on the recrystallization texture and mechanism of Al–Zn–Mg alloys, J. Alloys Compd. 580 (2013) 412–426.

[15] L. Zou, Q.L. Pan, Y.B. He, C.Z. Wang, W.J. Liang, Effect of minor Sc and Zr addition on microstructures and mechanical properties of Al–Zn–Mg–Cu alloys, Trans. Nonferrous Metals Soc. China 17 (2007) 340–345.

[16] L.L. Rokhlin, T.V. Dobatkina, N.R. Bochvar, E.V. Lysova, Investigation of phase equilibria in alloys of the Al–Zn–Mg–Cu–Zr–Sc system, J. Alloys Compd. 367 (2004) 10–16.

[17] H.C. Fang, H. Chao, K.H. Chen, Effect of Zr, Er and Cr additions on microstructures and properties of Al–Zn–Mg–Cu alloys, Mater. Sci. Eng. A-Struct. 610 (2014) 10–16.

[18] G.S. Peng, K.H. Chen, H.C. Fang, S.Y. Chen, Effect of Cr and Yb additions on microstructure and properties of low copper Al–Zn–Mg–Cu–Zr alloy, Mater. Design 36 (2012) 279–283.

[19] X.M. Li, M.J. Starink, Identification and analysis of intermetallic phases in overaged Zr-containing and Cr-containing Al–Zn–Mg–Cu alloys, J. Alloys Compd. 509 (2011) 471–476.

[20] T. Ogura, T. Otani, A. Hirose, T. Sato, Improvement of strength and ductility of an Al–Zn–Mg alloy by controlling grain size and precipitate microstructure with Mn and Ag addition, Mater. Sci. Eng. A-Struct. 580 (2013) 288–293.

[21] D.X. Yang, X.Y. Li, D.Y. He, H. Hui, Z. Liang, Study on microstructure and mechanical properties of Al–Mg–Mn–Er alloy joints welded by TIG and laser beam, Mater. Design 40 (2012) 117–123.

[22] Y.H. Cai, R.G. Liang, Z.P. Su, J.S. Zhang, Microstructure of spray formed Al–Zn–Mg–Cu alloy with Mn addition, Trans. Nonferrous Metals Soc. China 21 (2011) 9–14.

[23] Y.D. He, X.M. Zhang, Z.Q. Cao, Effect of minor Cr, Mn, Zr, Ti and B on grain refinement of as-cast Al–Zn–Mg–Cu alloys, Rare Metal Mater. Eng. 39 (2010) 1135–1140.

[24] L.K. Berg, J. Gjonnes, V. Hansen, X.Z. Li, M. Knutson-Wedel, G. Waterloo, et al., GP-zones in Al–Zn–Mg alloys and their role in artificial aging, Acta Mater. 49 (2001) 3443–3451.

[25] J.Q. Guo, K. Ohtera, An intermediate phase appearing in L1(2)-Al3Zr to DO23-Al3Zr phase transformation of rapidly solidified Al–Zr alloys, Mater. Lett. 27 (1996) 343–347.

[26] X.Z. Li, V. Hansen, J. Gjonnes, L.R. Wallenberg, HREM study and structure modeling of the eta′ phase, the hardening precipitates in commercial Al–Zn–Mg alloys, Acta Mater. 47 (1999) 2651–2659.

[27] K. Stiller, P.J. Warren, V. Hansen, J. Angenete, J. Gjonnes, Investigation of precipitation in an Al–Zn–Mg alloy after two-step ageing treatment at 100 degrees and 150 degrees C, Mater. Sci. Eng. A-Struct. 270 (1999) 55–63.

[28] A.K. Vasudévan, R.D. Doherty, Grain boundary ductile fracture in precipitation hardened aluminum alloys, Acta Metall. 35 (1987) 1193–1219.